

Radio properties of ten nearby ultraluminous infrared galaxies with signatures of luminous buried active galactic nuclei

Takayuki J. Hayashi^{1,2} *, Yoshiaki Hagiwara³, and Masatoshi Imanishi¹

¹National Astronomical Observatory of Japan, 2-21-1 Osawa, Mitaka, Tokyo 181-8588, Japan

²Azabu Junior and Senior High School, 2-3-29 Motoazabu, Minato-ku, Tokyo 106-0046, Japan

³Toyo University, Hakusan 5-28-20, Bunkyo-ku, Tokyo 112-8606, Japan

16 April 2021

ABSTRACT

We present the results of our multifrequency observations for 10 ultraluminous infrared galaxies (ULIRGs) made by the Karl G. Jansky Very Large Array at 1.4, 5.5, 9.0, and 14.0 GHz. Our sample is selected from ULIRGs whose active galactic nuclei (AGNs) are not found at optical wavelengths ($\sim 70\%$ of the entire ULIRGs), but whose presence is suggested by mid-infrared or submillimetre observations ($> 50\%$ of the non-AGN ULIRGs at optical wavelengths). The statistical properties of the targets are similar to those of the entire ULIRG sample, which implies that ULIRGs have common radiative processes regardless of the presence of optical AGNs, and thus AGNs might equally contribute to the radio emission of every ULIRG. Although their spectra are mainly explained by starbursts and/or merger activity, some individual sources suggest contributions from AGNs. IRAS 00188–0856, whose optical morphology is not disturbed, shows a large nonthermal fraction and a spectral break at high frequency, which can be explained by synchrotron ageing of nonthermal plasma emitted from AGNs. In addition, we find 100-kpc scale extended emission associated with IRAS 01004–2237. The two-sided morphology and absence of extended X-ray emission suggest that this system is not induced by a merger in a cluster but originates from AGN activity.

Key words: galaxies: active — galaxies: nuclei — radio continuum: galaxies — techniques: interferometric

1 INTRODUCTION

Galaxies with large infrared luminosities greater than $10^{12}L_{\odot}$ are known as ultraluminous infrared galaxies (ULIRGs; Sanders & Mirabel 1996), whose powerful energy sources are hidden behind infrared-emitting dust heated by energetic radiation from starbursts and/or active galactic nuclei (AGNs). Currently, there is a debate as to whether starbursts or AGNs are more energetically important. This is closely linked to understanding the history of star formation and the growth of supermassive black holes in the dust-obscured galaxy population in the early Universe. Unlike optically identifiable AGNs surrounded by torus-shaped dust (optical Seyferts; Veilleux & Osterbrock 1987; Kewley et al. 2001; Kauffmann et al. 2003), ULIRGs are systems of major mergers and contain large amounts of concentrated molecular gas and dust in their nuclei (Sanders & Mirabel 1996). The putative compact AGNs at ULIRG’s nuclei can thus be completely obscured by the gas and dust in all directions. Therefore, while $\sim 30\%$ of ULIRGs are classified as Seyfert (Veilleux et al. 1999), this situation makes optical detection of AGN signatures difficult. Hence, the existence of elusive buried AGNs is presumed (Maiolino et al. 2003; Imanishi et al. 2006).

To investigate elusive buried AGNs in ULIRG’s nuclei, it is critical to observe the wavelengths where the effects of dust extinction are small. Based on spectroscopy at the mid-infrared (MIR) band of 3–35 μm , buried AGNs are distinguished from normal starbursts and have also been identified in more than half of ULIRGs, where

no AGNs are found at optical wavelengths (Armus et al. 2004, 2007; Imanishi et al. 2007, 2008, 2010a,b; Imanishi 2009; Nardini et al. 2008, 2009, 2010; Veilleux et al. 2009). Although it is considered physically extreme (Soifer et al. 2000; Thompson et al. 2005; Imanishi et al. 2007), starbursts highly concentrated in the centre may show infrared spectra similar to those of buried AGNs (Spoon et al. 2004). Thus, the energetic contribution of AGNs has not been firmly established yet. Furthermore, recent submillimetre observations report a high flux-density ratio of HCN to HCO⁺ emission, suggesting that deeply buried AGNs are present in ULIRGs even without signatures of AGNs at MIR (Imanishi et al. 2016, 2018, 2019). There is a physical limitation to scrutinise ULIRG’s nuclei by infrared observations alone. Hence, we require observations at another wavelength, such as radio wave, where dust is more transparent than at infrared or submillimetre wavelengths.

In this study, we focus on radio spectra of ULIRGs. Radio emission from ULIRGs is a mixture of those originating from thermal and nonthermal plasma, where the former originates from star formation while the latter is also related to AGNs (Condon et al. 1991). In the GHz range, although an optically thin steep spectrum is produced by nonthermal plasma in supernova remnants, it sometimes becomes peaked or inverted in AGNs if synchrotron self-absorption (SSA) owing to a strong magnetic field is present (e.g. Tornaiainen et al. 2005; Orienti & Dallacasa 2008). Moreover, the large bulk Lorentz factor of a collimated jet from AGNs can cause strong variability (Lister 2001). Thus, the presence of AGNs can be confirmed by studying the spectral shape and flux-density variation. In addition, while typical ULIRGs show steep spectra with flattening

* Contact-mail: t.hayashi@nao.ac.jp

at low and high frequencies caused by free-free absorption (FFA) and free-free emission (FFE) due to thermal plasma, respectively (Condon et al. 1991; Clemens et al. 2008, 2010; Leroy et al. 2011; Galvin et al. 2018; Murphy 2013), some sources suggest steepening at high frequency. While Clemens et al. (2010) and Murphy (2013) consider starbursts and merger activity as the origin, respectively, synchrotron ageing of nonthermal plasma produced by AGNs can also naturally explain the steepening, which is proposed as a way to distinguish AGNs (Leroy et al. 2011).

To examine the statistical impact of the AGNs on the radio spectra through comparison with previous observations, and to validate the AGN diagnosis by discussing the origin of the radio spectra, we present the results of multifrequency observations conducted with the Karl G. Jansky Very Large Array (VLA). While previous studies were intended for the entire set of ULIRGs (Condon et al. 1991; Clemens et al. 2008, 2010; Leroy et al. 2011; Murphy 2013), in this paper, we observe ULIRGs hosting buried AGNs identified by MIR or submillimetre spectroscopy but no evidence of AGNs at optical wavelengths (Imanishi et al. 2007, 2016, 2018, 2019; Imanishi & Nakanishi 2014). We describe our sample sources in Section 2, the observations and data reduction in Sections 3, and the results in Section 4. Section 5 discusses the origin of the radio properties, including the spectra. Finally, our conclusions are summarised in Section 6. In this paper, we define the spectral index, α , as $f_\nu \propto \nu^\alpha$, where f_ν is flux density at frequency, ν . In this definition, a steep spectrum is represented by $\alpha < 0$.

2 SAMPLE

Table 1 lists our sample. We selected the sample from nearby ULIRGs that show positive AGN signatures in Imanishi et al. (2007). Their sample consists of 48 ULIRGs at $z < 0.15$ from the IRAS 1 Jy sample (Kim & Sanders 1998), whose optical classification is LINER or H II (Veilleux et al. 1999). They classify the ULIRGs into four levels based on the strength of the AGN sign presented by MIR spectroscopy. Of 26 ULIRGs with some AGN signatures, we selected nine ULIRGs whose R.A. are ranged 22 to 5 hour. In addition, for all but two (IRAS 00482–2721, IRAS 23327+2913) of the sample submillimetre spectroscopy is performed by Imanishi et al. (2019), where the presence of buried AGNs is suggested by an HCN-to-HCO⁺ ($J = 3-2$) flux-density ratio higher than unity. Table 2 shows the result of the AGN diagnostics.

In this study, we also added IRAS 22491–1808, whose MIR spectral feature of the source implies a strong starburst sign, to our sample because the source is considered to contain deeply buried AGN that was elusive at even MIR (Imanishi & Nakanishi 2014; Imanishi et al. 2016, 2018, 2019). IRAS 22491–1808 shows a high HCN-to-HCO⁺ flux-density ratio similar to that of AGN-dominated ULIRGs and a ratio of the vibrationally excited HCN emission line to the vibrational ground emission line higher than the starburst galaxies, which is presumed to be produced by hot dust heated by the AGN.

3 OBSERVATION AND DATA REDUCTION

Our multifrequency JVLA observations were made between October 2015 and August 2016 (project codes: AH1185 and AH1196). To make observations with a similar u - v range at different bands, we utilised the B, C, C, and D configurations for observations at the L, C, X, and Ku bands, respectively (the D configuration is the most compact). Table 3 shows an observational summary. As presented

in the VLA status summary at the time, the typical largest angular scales are 60, 120, 70, and 50 arcsec for snapshot images at the L, C, X, and Ku bands, respectively.

We reduced the data using the Common Astronomy Software Applications (CASA; McMullin et al. 2007) package developed by the National Radio Astronomy Observatory (NRAO). We calibrated the bandpass, phase, and amplitude response of individual antennas with a standard procedure. During the calibration, we flagged bad data based on the signal-to-noise ratio of visibilities. All data in each band were combined into a single image using CASA’s multi-term multifrequency synthesis capabilities with a Briggs weighting setting $\text{robust} = 0.5$. We set a reference frequencies of output images at the C, X, and Ku bands as 5.5 GHz, 9.0 GHz, and 14.0 GHz, respectively, which are default values of CASA calculated as the middle of the observed frequency ranges. For the L band, we manually set reference frequency of 1.4 GHz to evaluate flux-density variation by comparing the flux density with prior survey observations made at the same frequency (Becker et al. 1995; Condon et al. 1998). We also conducted phase-only self-calibration of the data whenever possible. Table 4 shows the resolution and noise level of each image.

The images of each source were restored by a beam of the lowest resolution image. We measured the flux densities of the targets by CASA’s task IMFIT, which fit an elliptical Gaussian component within a small box containing a radio source. We estimated the flux-density errors by the root sum square of the error presented by IMFIT, which contains thermal noise and fitting errors, and a nominal calibration uncertainty of 5% presented in the VLA status summary at the time.

4 RESULTS

4.1 Radio Spectrum and Morphology

Table 5 lists the results of the flux-density measurements and derived spectral indices of our targets. In images at all bands, all targets but one show a pointlike structure. The one exception is IRAS 01004–2237, whose image is displayed in Figure 1. The radio emission of the source spreads symmetrically over ~ 50 arcsec toward the southwest and northeast. Because 1 arcsec corresponds to ~ 2 kpc at the redshift, its projected linear size is ~ 100 kpc. The values of IRAS 01004–2237 shown in Table 5 are the result of the core. Also note that, since IRAS 04103–2838 was observed only in the L and Ku bands, we only obtained a spectral index between 1.4 and 14.0 GHz, whose value is -0.87 ± 0.03 .

Murphy et al. (2013) have reported that ULIRGs with extremely low 6.2- μm PAH equivalent width of $\text{EW}_{6.2}^{\text{PAH}} < 100$ nm, which suggests the presence of buried AGNs, did not have a spectral index between 1.5 and 8.4 GHz steeper than -0.6 . By contrast, we find that IRAS 00188–0856, whose $\text{EW}_{6.2}^{\text{PAH}}$ is 85 nm, shows both $\alpha_{5.5}^{1.4}$ and $\alpha_{9.0}^{5.5}$ steeper than -0.8 .

Figure 2 displays radio spectra of the targets, where data points obtained by previous survey observations (NVSS; Condon et al. 1998, and the FIRST survey; Becker et al. 1995) are also indicated. Generally, radio emission of starburst galaxies comes from a mixture of thermal and nonthermal plasma suffering from absorption by thermal plasma. Thus, assuming a uniform free-free optical depth, the radio brightness of a starburst galaxy is modelled by

$$f_\nu \propto T_e (1 - e^{-\tau_\nu}) \left[1 + \frac{1}{H} \left(\frac{\nu}{\text{GHz}} \right)^{0.1 + \alpha_0} \right] \nu^2, \quad (1)$$

where T_e and $\tau_\nu \propto \nu^{-2.1}$ are the electron temperature and optical

Table 1. ULIRG Sample for VLA Observation.

ID	Object	R.A. (J2000)	Dec. (J2000)	z	$\log L_{\text{IR}}$ (L_{\odot})	Optical Class	J (mag)	K (mag)
(1)	(2)	(3)	(4)	(5)	(6)	(7)	(8)	(9)
1	IRAS 00091–0738	00 11 43.25	−07 22 07.5	0.118	12.19	H II	15.34 ± 0.05	13.96 ± 0.07
2	IRAS 00188–0856	00 21 26.48	−08 39 27.1	0.128	12.33	LINER	15.18 ± 0.08	13.26 ± 0.04
3	IRAS 00482–2721	00 50 40.37	−27 04 38.8	0.129	12.00	LINER	16.04 ± 0.18	15.04 ± 0.39
4	IRAS 01004–2237	01 02 49.92	−22 21 57.0	0.118	12.24	H II	16.10 ± 0.14	14.34 ± 0.14
5	IRAS 01166–0844	01 19 07.54	−08 29 09.4	0.118	12.03	H II	15.72 ± 0.12	14.54 ± 0.28
6	IRAS 01298–0744	01 32 21.41	−07 29 08.9	0.136	12.27	H II	16.33 ± 0.26	14.95 ± 0.30
7	IRAS 04103–2838	04 12 19.47	−28 30 24.4	0.118	12.15	LINER	14.78 ± 0.07	13.29 ± 0.04
8	IRAS 21329–2346	21 35 45.86	−23 32 35.6	0.125	12.09	LINER	15.52 ± 0.03	14.25 ± 0.07
9	IRAS 22491–1808	22 51 49.23	−17 52 22.9	0.076	12.09	H II	14.50 ± 0.05	13.31 ± 0.09
10	IRAS 23327+2913	23 35 11.92	+29 30 00.4	0.107	12.06	LINER	15.16 ± 0.07	13.60 ± 0.07

Columns are as follows: (1) Object ID; (2) IRAS source name; (3)(4) Optical positions; (5) Redshift; (6) Infrared luminosity; Reference for the columns (2)–(6) are [Kim & Sanders \(1998\)](#). (7) Optical classification ([Veilleux et al. 1999](#)); (8)(9) J - and K -band aperture magnitudes from the 2MASS all sky survey ([Cutri et al. 2003](#); [Skrutskie et al. 2006](#)). The observed wavelengths of the J and K bands in the survey are 1.25 and 2.16 μm , respectively.

Table 2. AGN diagnoses of the sample.

Object	$\text{EW}_{6.2}^{\text{PAH}}$ (nm)	$\text{EW}_{7.7}^{\text{PAH}}$ (nm)	$\text{EW}_{11.3}^{\text{PAH}}$ (nm)	$\tau_{9.7}$	$\tau_{18}/\tau_{9.7}$	$\tau'_{18}/\tau_{9.7}$	HCN/HCO^+ ($J = 3-2$)
(1)	(2)	(3)	(4)	(5)	(6)	(7)	(8)
IRAS 00091–0738	50	350	255	3.2	0.33	0.39	1.6 ± 0.3
IRAS 00188–0856	85	305	290	2.5	0.22	0.26	1.9 ± 0.2
IRAS 00482–2721	260	710	465	2.1	0.29	0.36	...
IRAS 01004–2237	45	190	8	0.4	1.0 ± 0.2
IRAS 01166–0844	30	430	190	3.0	0.25	0.30	1.6 ± 0.3
IRAS 01298–0744	10	380	155	4.0	0.27	0.34	1.3 ± 0.2
IRAS 04103–2838	165	365	120	0.6	1.2 ± 0.3
IRAS 21329–2346	230	635	370	2.2	0.9 ± 0.2
IRAS 22491–1808	325	695	460	1.5	2.3 ± 0.2
IRAS 23327+2913	255	485	175	1.3	1.0 ± 0.2

Columns are as follows: (1) IRAS source name; (2)–(4) Rest-frame equivalent width of PAH emission at 6.2, 7.7, and 11.3 μm , respectively. Positive AGN signatures are indicated in bold font, based on the low equivalent width of $\text{EW}_{6.2}^{\text{PAH}} < 180$ nm, $\text{EW}_{7.7}^{\text{PAH}} < 230$ nm, and $\text{EW}_{11.3}^{\text{PAH}} < 200$ nm; (5) Optical depth of silicate dust absorption feature at 9.7 μm , against a power-law continuum determined from data points at 7.1 and 14.2 μm . Positive AGN signatures are indicated in bold font, based on the high optical depth of $\tau_{9.7} > 2$; (6)(7) ratio of optical depth of silicate dust absorption feature at 18 μm to that at 9.7 μm , which represents dust temperature gradients. τ_{18} and τ'_{18} are the optical depths against a power-law continuum determined from data points at 14.2 and 24 μm , and 14.2 and 29 μm , respectively. Positive AGN signatures are indicated in bold font, based on strong dust temperature gradients determined by $\tau_{18}/\tau_{9.7} < 0.27$ and $\tau'_{18}/\tau_{9.7} < 0.32$; Reference for the columns (2)–(7) is [Imanishi et al. \(2007\)](#). (8) HCN-to-HCO⁺ ($J = 3-2$) flux-density ratio. Values at the nuclear peak position within the beam (typically ~ 0.2 arcsec) are shown. Positive AGN signatures are indicated in bold font, based on the ratio higher than unity. References for the column (8) are [Imanishi et al. \(2016, 2019\)](#).

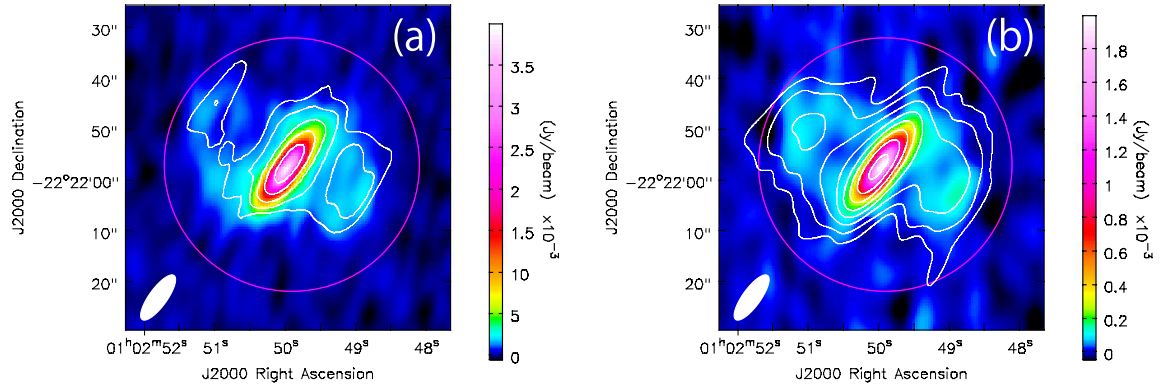
Table 3. Observation Summary.

Band	Centre Frequencies	Bandwidth	Configuration	Date	Observed targets
L	1.25 and 1.75 GHz	512 MHz each	B	2016 July 08	5, 6, 7
				2016 August 19	1, 2, 3, 4, 8, 9, 10
C	5.0 and 6.0 GHz	1024 MHz each	C	2016 March 19	1, 2, 3, 4, 5, 6, 8, 9, 10
X	8.5 and 9.5 GHz	1024 MHz each	C	2016 March 18	1, 2, 3, 4, 5, 6, 8, 9, 10
Ku	13.0 and 15.0 GHz	1024 MHz each	D	2015 October 18	9, 10
				2015 October 19	1, 2
				2015 October 20	3, 4, 5, 6, 7, 8

Numbers in observed targets column are object IDs in Table 1.

Table 4. Synthesised beam and r.m.s noise level of the images.

Object	1.4 GHz			5.5 GHz			9.0 GHz			14.0 GHz		
	Beam size (arcsec ²)	P.A. (deg)	r.m.s ($\mu\text{Jy beam}^{-1}$)	Beam size (arcsec ²)	P.A. (deg)	r.m.s ($\mu\text{Jy beam}^{-1}$)	Beam size (arcsec ²)	P.A. (deg)	r.m.s ($\mu\text{Jy beam}^{-1}$)	Beam size (arcsec ²)	P.A. (deg)	r.m.s ($\mu\text{Jy beam}^{-1}$)
IRAS 00091–0738	7.2×3.9	140	67	4.8×3.3	174	25	3.2×2.2	163	19	9.9×4.5	134	18
IRAS 00188–0856	7.8×3.9	141	78	5.0×3.5	173	16	3.5×2.0	149	16	9.6×4.4	135	17
IRAS 00482–2721	13.6×3.6	148	49	8.3×3.2	167	16	5.5×2.0	158	16	10.1×4.5	4	13
IRAS 01004–2237	13.0×4.7	143	71	7.9×3.6	167	18	4.9×2.1	157	17	10.2×4.8	4	17
IRAS 01166–0844	5.8×4.6	31	51	5.4×3.7	153	15	3.6×2.1	151	14	7.1×5.3	15	12
IRAS 01298–0744	5.7×3.6	41	82	5.3×3.4	157	15	3.7×2.1	146	14	6.9×5.0	19	12
IRAS 04103–2838	8.1×4.0	1	62	12.1×4.7	162	15
IRAS 21329–2346	7.9×4.7	164	199	8.0×3.4	21	17	4.4×2.1	10	16	8.4×3.9	169	17
IRAS 22491–1808	7.3×4.1	144	74	6.2×3.8	9	17	3.7×2.1	174	15	7.8×4.2	154	18
IRAS 23327+2913	4.9×3.7	125	67	4.4×3.4	36	19	2.2×2.1	45	15	6.2×5.5	110	17

**Figure 1.** Radio images of IRAS 01004–2237 convolved with a synthesised beam of the observation at 1.4 GHz that is 13.0×4.7 arcsec² at a position angle of 143 degree. Circles coloured by magenta with a radius of 50 arcsec are regions for obtaining integrated flux density of extended emission. (a) Image at 5.5 GHz with 1.4-GHz contours overlaid. Contour levels begin at $231 \mu\text{Jy beam}^{-1}$ (3σ noise level of the image) and are spaced by a factor of 2. (b) Image at 14.0 GHz with 9.0-GHz contours overlaid. Contour levels begin at $58 \mu\text{Jy beam}^{-1}$ (3σ noise level of the image) and are spaced by a factor of 2.**Table 5.** Flux densities and spectral indices of cores obtained by our new VLA observations.

Object	Convolved beam (arcsec ²)	P.A. (deg)	$f_{1.4}$ (mJy)	$f_{5.5}$ (mJy)	$f_{9.0}$ (mJy)	$f_{14.0}$ (mJy)	$\alpha_{5.5}^{1.4}$	$\alpha_{9.0}^{5.5}$	$\alpha_{14.0}^{9.0}$
(1)	(2)	(3)	(4)	(5)	(6)	(7)	(8)	(9)	(10)
IRAS 00091–0738	9.9×4.5	134	4.73 ± 0.34	3.60 ± 0.19	2.96 ± 0.15	2.03 ± 0.11	-0.20 ± 0.07	-0.40 ± 0.15	-0.85 ± 0.17
IRAS 00188–0856	9.6×4.4	135	20.26 ± 1.23	6.70 ± 0.34	4.32 ± 0.22	2.74 ± 0.14	-0.81 ± 0.06	-0.89 ± 0.14	-1.03 ± 0.16
IRAS 00482–2721	13.6×3.6	149	6.54 ± 0.35	2.67 ± 0.14	1.75 ± 0.09	1.28 ± 0.07	-0.65 ± 0.05	-0.86 ± 0.15	-0.71 ± 0.17
IRAS 01004–2237	13.0×4.7	143	8.40 ± 0.50	4.79 ± 0.31	3.25 ± 0.19	2.45 ± 0.15	-0.41 ± 0.06	-0.79 ± 0.18	-0.64 ± 0.19
IRAS 01166–0844	7.1×5.3	15	1.27 ± 0.13	0.72 ± 0.04	0.42 ± 0.02	0.43 ± 0.03	-0.41 ± 0.09	-1.07 ± 0.16	$+0.03 \pm 0.21$
IRAS 01298–0744	6.9×5.0	19	4.22 ± 0.53	3.51 ± 0.18	3.15 ± 0.16	2.61 ± 0.13	-0.14 ± 0.10	-0.22 ± 0.14	-0.43 ± 0.16
IRAS 04103–2838	12.1×4.7	162	13.35 ± 0.75	1.79 ± 0.09
IRAS 21329–2346	8.4×3.9	169	9.34 ± 0.70	3.34 ± 0.17	2.14 ± 0.11	1.59 ± 0.08	-0.75 ± 0.07	-0.90 ± 0.15	-0.67 ± 0.17
IRAS 22491–1808	7.8×4.2	154	6.62 ± 0.40	4.05 ± 0.21	3.28 ± 0.17	2.66 ± 0.14	-0.36 ± 0.06	-0.43 ± 0.15	-0.47 ± 0.16
IRAS 23327+2913	6.2×5.5	110	8.46 ± 0.46	3.26 ± 0.16	2.12 ± 0.11	1.49 ± 0.08	-0.70 ± 0.05	-0.87 ± 0.14	-0.81 ± 0.16
average	-0.54 ± 0.02	-0.71 ± 0.05	-0.65 ± 0.06

Columns are as follows: (1) IRAS source name; (2)(3) Convolved beam size and position angle; (4)–(7) Flux densities at 1.4, 5.5, 9.0, and 14.0 GHz, respectively; (8)–(10) Spectral indices between neighbouring bands. We obtained flux densities only at 1.4 and 14.0 GHz for IRAS 04103–2838, whose spectral index between the frequencies is -0.87 ± 0.03 . The average of spectral indices weighted by the measurement error is also presented in each frequency range, whose error represents standard error on the mean.

depth of the thermal plasma, respectively, and H is a ratio of the thermal to nonthermal components (Condon et al. 1991). In this model, if $\tau_\nu \ll 1$, then we obtained $(1 - e^{-\tau_\nu}) \sim \tau_\nu$. Thus, $f_\nu \sim \nu^{-0.1}$ if the thermal component is dominant, while $f_\nu \sim \nu^\alpha$ if the thermal component is negligible. We fit this model to the obtained spectra, which is also shown in Figure 2. Because our observations provide only four data points, we fix $\alpha_0 = -0.8$, which is a typical value of nonthermal synchrotron emission. In the figure, we also illustrate the thermal and nonthermal components of the model.

We also provide the average of spectral indices in each frequency range in Table 5. The spectral index between two frequencies, ν_1 and ν_2 , is now described as $\alpha_{\nu_2}^{\nu_1}$. We find that the average $\alpha_{5.5}^{1.4}$ is significantly less negative (i.e. flatter) than $\alpha_{9.0}^{5.5}$, while no significant difference is found between $\alpha_{9.0}^{5.5}$ and $\alpha_{14.0}^{9.0}$. That is, flattening of the spectrum is discovered only in the lowest frequency range but not in the higher frequency range. Figure 3 shows a comparison between $\alpha_{5.5}^{1.4}$ and $\alpha_{14.0}^{9.0}$, which suggests no significant correlation at 95% significance. These trends are similar to previous reports for the entire ULIRGs (Clemens et al. 2008; Murphy 2013; Galvin et al. 2018), which will be discussed in Section 5.1.

In Figure 4, we show the radio spectrum of the extended emission associated with IRAS 01004–2237. Flux-density measurements were made by subtracting the core emission obtained by IMFIT from the integrated flux density within 50 arcsec of the centre (see also Figure 1). We also illustrate the best-fit model provided by Equation 1. We will discuss the origin of this feature in Section 5.3.3

4.2 Flux-density variation

To evaluate the significance of flux-density variability, we utilise the following index introduced by Zhou et al. (2006),

$$\sigma_{\text{var}} = \frac{|S_1 - S_2|}{\sqrt{\sigma_1^2 + \sigma_2^2}}, \quad (2)$$

where S_i and σ_i are the flux density and uncertainty of the i -th epoch data, respectively. Objects with $\sigma_{\text{var}} > 3$ are candidates for variable sources (Zhou et al. 2006; Ghosh & Punjly 2007). We compare the flux density at 1.4 GHz obtained by our new observations with those from previous survey observations (NVSS and the FIRST survey). Both survey observations do not present the flux-density errors with calibration uncertainty, which now we assume 5% of the total flux density as we did for our observations. When we compare data measured with different array configurations, sources that suggest peak flux density at a high resolution larger than integrated flux density at lower resolution are considered as possible variable objects. Now, because our observations and the FIRST survey utilised the B configuration while NVSS was conducted with the D configuration, the resolution of our observation (~ 5 arcsec) is comparable with the FIRST survey, but higher than NVSS (~ 45 arcsec).

Table 6 presents the results. While IRAS 01004–2237 showing the extended emission (Figure 1) indicates $\sigma_{\text{var}} > 3$ in comparison with NVSS, this large deviation comes from the effect of array configurations. On the other hand, the other comparisons show $\sigma_{\text{var}} < 3$. Although these two-epoch comparisons are not enough to conclude that the sources are stable, we do not find significant flux-density variation for our targets. This finding suggests that, while our multi-band observations were not made simultaneously, radio spectra and spectral indices presented in Section 4.1 are physically meaningful for the following discussions.

4.3 Radio spectral indices and FIR-to-radio ratio

Table 7 shows FIR-to-radio ratio, q_ν , and related FIR properties obtained by IRAS observations. Here, q_ν is defined as follows: $q_\nu = \log[(f_{\text{FIR}}/3.75 \times 10^{12} \text{ Hz})/f_\nu]$, where f_{FIR} is the FIR flux density in units of $\text{W m}^{-2} \text{ Hz}^{-1}$ commonly defined as $f_{\text{FIR}} = 1.26 \times 10^{14} (2.58 \times f_{60} + f_{100})$ (Helou et al. 1985). To compare FIR emission with intrinsic radio power, we utilise flux density at 9.0 GHz, where emission is free from absorption in most of the sources (see Figure 2). Table 7 also lists FIR-to-radio ratio at 1.4 GHz after correction for FFA, $q'_{1.4}$, introduced by Condon et al. (1991), which is now defined as $q'_{1.4} = q_{1.4} + (\alpha_0 - \alpha_{5.5}^{1.4}) \log(5.5/1.4)$. They find that galaxies with large infrared luminosities of $\geq 10^{12} L_\odot$ have a distribution of $q'_{1.4}$ narrower than that of $q_{1.4}$. Our sample shows a similar trend, where the scatter of $q_{1.4}$ and $q'_{1.4}$ are 0.30 and 0.22, respectively. Now, the scatter of $q_{9.0}$ is 0.23, which suggests that $q_{9.0}$ behaves in the same way as $q'_{1.4}$. Since $q_{9.0}$ is calculated without assuming the true value of α_0 , we will use $q_{9.0}$ in our discussion.

Figure 5 shows the plot of the radio spectral indices against $q_{9.0}$. We find a significant correlation between $\alpha_{14.0}^{9.0}$ and $q_{9.0}$ at the 95% confidence level, while no significant correlation is found if $\alpha_{5.5}^{1.4}$ is considered instead. Thus, a large $q_{9.0}$ is associated with sources showing $\alpha_{14.0}^{9.0} \sim 0$, which suggests a flat spectrum. In the figure, we also show data points for the entire ULIRGs provided by Clemens et al. (2008). Although their observed frequencies are different from ours, both results suggest that correlation with FIR-to-radio ratio is significantly stronger at higher frequencies than at lower frequencies.

4.4 Radio spectral indices and FIR colour

Figure 6 shows the plot of the radio spectral indices against the FIR colour, f_{60}/f_{100} , from IRAS observations. We find a significant correlation between $\alpha_{5.5}^{1.4}$ and f_{60}/f_{100} at the 95% confidence level, while no correlation is found if $\alpha_{14.0}^{9.0}$ is considered instead. Thus, a large f_{60}/f_{100} is associated with sources showing $\alpha_{5.5}^{1.4} \sim 0$, which suggests a flat spectrum. Because f_{60}/f_{100} is a measure of dust temperature heated by starbursts, whose large value indicates high dust temperature and then active star formation, ULIRGs with strong starbursts are accompanied by a flat spectrum at lower frequencies more often than at higher frequencies. In the figure, we also show data points for the entire ULIRGs provided by Clemens et al. (2008). Although their observed frequencies are different from ours, both results suggest that correlation with FIR colour is significantly stronger at lower frequencies than at higher frequencies.

4.5 Radio spectral indices and near-infrared colour

In Figure 7, we plot the radio spectral indices against the near-infrared (NIR) colour index, $(J - K)$, derived from the results of the 2MASS survey (Skrutskie et al. 2006). At the 95% confidence level, the radio spectral indices in both low and high frequencies, $\alpha_{5.5}^{1.4}$ and $\alpha_{14.0}^{9.0}$, are not significantly correlated with $(J - K)$ that becomes large when galaxies shroud hot dust of 150–250 K heated by AGNs. In Figure 6, we also show data points for the entire ULIRGs provided by Clemens et al. (2008). Although their observed frequencies are different from ours, both results suggest that correlation with NIR colour is not significant at both high and low frequencies.

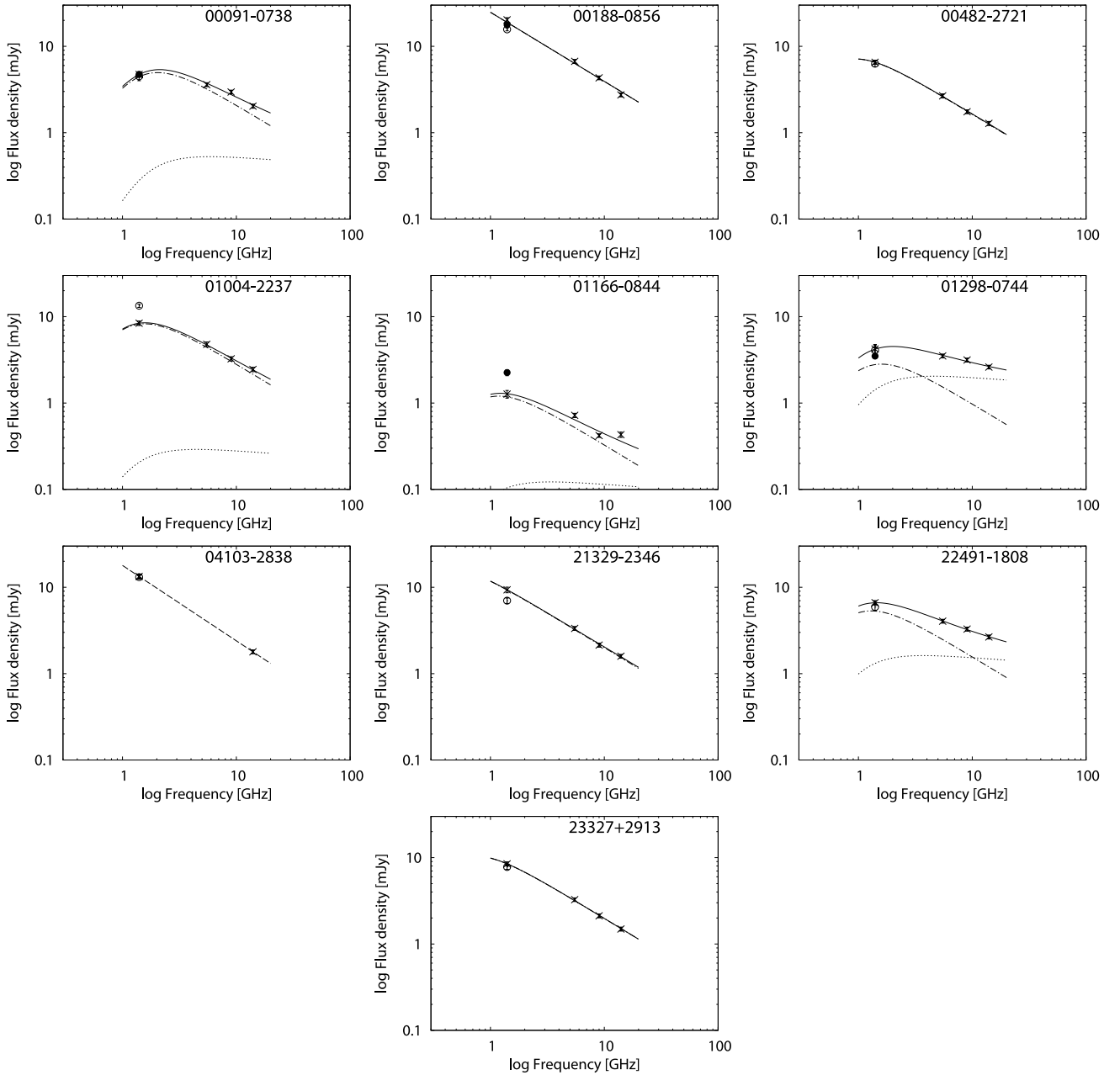


Figure 2. Radio spectra of the targets obtained by our observations. Observed data (crosses) and best-fit model for the spectra presented by Equation 1 are indicated. We also show data points from the FIRST survey (filled circles; Becker et al. 1995) and NVSS (open circles; Condon et al. 1998). The model has a nonthermal component absorbed by thermal plasma with free-free emission. The thermal component (dotted line) and the nonthermal component (dot-dashed line) are also indicated. For IRAS 04103–2838, we made observations only at two bands, which is insufficient to fit the model. Hence, a simple power law fit is indicated (dashed line). Because IRAS 00188–0856, IRAS 00482–2721, IRAS 21329–2346, and IRAS 23327+2913 show a small thermal fraction, their thermal components are not illustrated in the panels, and the solid line overlaps the dot-dashed line.

5 DISCUSSIONS

5.1 Comparison with overall ULIRGs sample

Our new VLA observations provide spectral properties of ULIRGs whose presence of AGNs is suggested by MIR or submillimetre spectroscopy but no sign of AGN at optical wavelengths (Imanishi et al. 2007, 2016, 2018, 2019; Imanishi & Nakanishi 2014). Previously, Clemens et al. (2008) made multifrequency observations for the overall ULIRG sample selected from the IRAS Bright Galaxy Sample (Soifer et al. 1989). A comparison between their results and ours

would provide new insight to reveal the origin of the radio emission and the heating sources of the dust in ULIRGs.

The main results of our observations are as follows: The spectral indices at low and high frequencies ($\alpha_{5.0}^{1.4}$ and $\alpha_{14.0}^{9.0}$) do not relate to each other (Figure 3). The FIR-to-radio ratio at 9.0 GHz, $q_{9.0}$, significantly correlates with the spectral index at high frequency, $\alpha_{14.0}^{9.0}$, while no relation is found at low frequency (Figure 5). In contrast, the FIR colour, f_{60}/f_{100} , significantly correlates with the spectral index at low frequency, $\alpha_{5.0}^{1.4}$, while no relation is found at high frequency (Figure 6). These trends are similar to the results obtained

Table 6. Significance of flux-density variability.

Object	$f_{1.4}^{\text{NVSS}}$ (mJy)	$J_{1.4}^{\text{FIRST}}$ (mJy beam ⁻¹)	NVSS-FIRST	ours-NVSS	ours-FIRST
(1)	(2)	(3)	(4)	(5)	(6)
IRAS 00091–0738	4.5 ± 0.9	5.0 ± 0.4	0.78	0.34	0.34
IRAS 00188–0856	15.7 ± 1.2	17.2 ± 1.6	0.84	1.97	1.60
IRAS 00482–2721	6.3 ± 0.9	0.05	...
IRAS 01004–2237	13.4 ± 1.1	6.77	...
IRAS 01166–0844	...	1.3 ± 0.3	2.82
IRAS 01298–0744	4.1 ± 0.9	3.9 ± 0.8	0.15	1.21	0.91
IRAS 04103–2838	13.1 ± 1.1	0.51	...
IRAS 21329–2346	7.0 ± 0.9	0.25	...
IRAS 22491–1808	5.9 ± 0.9	0.16	...
IRAS 23327+2913	7.8 ± 0.9	0.55	...

Columns are as follows: (1) IRAS source name; (2) Integrated flux density at 1.4 GHz provided by NVSS (Condon et al. 1998); (3) Peak flux density at 1.4 GHz provided by the FIRST survey (Becker et al. 1995); (4)–(6) Significance of variability between NVSS and the FIRST survey, our observations and NVSS, and our observations and the FIRST survey, respectively.

Table 7. FIR-to-radio ratios.

Object	f_{12} (Jy)	f_{25} (Jy)	f_{60} (Jy)	f_{100} (Jy)	FIR (/10 ⁻¹³ W m ⁻²)	$q_{1.4}$	$q_{9.0}$	$q'_{1.4}$
(1)	(2)	(3)	(4)	(5)	(6)	(7)	(8)	
IRAS 00091–0738	0.07 ± 0.02	0.22 ± 0.05	2.63 ± 0.18	2.52 ± 0.20	1.17 ± 0.07	2.82 ± 0.04	3.02 ± 0.03	2.46 ± 0.07
IRAS 00188–0856	0.12 ± 0.04	0.37 ± 0.07	2.59 ± 0.23	3.40 ± 0.34	1.27 ± 0.09	2.22 ± 0.04	2.89 ± 0.04	2.23 ± 0.06
IRAS 00482–2721	0.11 ± 0.03	0.18 ± 0.05	1.13 ± 0.14	1.84 ± 0.17	0.60 ± 0.05	2.39 ± 0.04	2.96 ± 0.04	2.30 ± 0.06
IRAS 01004–2237	0.23 ± 0.07	0.66 ± 0.08	2.29 ± 0.16	1.79 ± 0.18	0.97 ± 0.06	2.49 ± 0.04	2.90 ± 0.04	2.26 ± 0.06
IRAS 01166–0844	0.14 ± 0.04	0.18 ± 0.04	1.74 ± 0.10	1.42 ± 0.24	0.74 ± 0.05	3.20 ± 0.05	3.67 ± 0.04	2.97 ± 0.09
IRAS 01298–0744	0.12 ± 0.03	0.28 ± 0.08	2.47 ± 0.15	2.08 ± 0.25	1.07 ± 0.06	2.83 ± 0.06	2.95 ± 0.03	2.43 ± 0.10
IRAS 04103–2838	0.08 ± 0.02	0.54 ± 0.04	1.82 ± 0.09	1.71 ± 0.17	0.81 ± 0.04	2.21 ± 0.03	2.91 ± 0.03	2.25 ± 0.04
IRAS 21329–2346	0.08 ± 0.02	0.16 ± 0.04	1.65 ± 0.08	2.22 ± 0.18	0.82 ± 0.03	2.37 ± 0.04	3.01 ± 0.03	2.34 ± 0.07
IRAS 22491–1808	0.12 ± 0.04	0.55 ± 0.07	5.44 ± 0.38	4.45 ± 0.36	2.33 ± 0.13	2.97 ± 0.04	3.28 ± 0.03	2.71 ± 0.06
IRAS 23327+2913	0.06 ± 0.02	0.23 ± 0.06	2.10 ± 0.13	2.81 ± 0.45	1.04 ± 0.07	2.51 ± 0.04	3.11 ± 0.04	2.45 ± 0.06
average	2.64 ± 0.01	3.09 ± 0.01	2.46 ± 0.02

Columns are as follows: (1) IRAS source name; (2)–(5) Flux densities at 12, 25, 60, and 100 μm , respectively (Moshir & et al. 1990); (6) FIR flux density as used to calculate the FIR-to-radio ratio, q ; (7)(8) FIR-to-radio ratios, q , at 1.4, and 9.0 GHz, respectively; (9) FIR-to-radio ratio at 1.4 GHz after correction for FFA, $q'_{1.4}$, introduced by Condon et al. (1991). The average of FIR-to-radio ratios weighted by the measurement error is also presented, whose error represents standard error on the mean. FIR-to-radio ratio of IRAS 04103–2838 in each column is calculated by interpolation from flux densities at 1.4 and 14.0 GHz, as required, but we exclude the values when the average are calculated.

by Clemens et al. (2008). For further comparison, composite spectra normalised at flux density in the C band are shown in Figure 8, where the model presented in Equation 1 is also illustrated. As for data from the previous study, we selected ULIRGs observed at the same bands as our observations (i.e. the L, C, X, and Ku bands). The overall spectral shapes and the models are comparable between the previous report and ours, and both observations at lower frequencies indicate flux scattering larger than at higher frequencies.

Considering that our targets are selected from H II and LINER nuclear classifications, the similarities mentioned above imply that radiative processes at radio wavelength might be common in both ULIRGs with and without AGN signatures at optical wavelengths, which is also reported by Murphy (2013). Since our targets indicate hints of buried AGNs by MIR or submillimetre spectroscopy, this means that radio emission from AGNs could be included in our sample as in the overall ULIRGs sample. Therefore, the results might confirm the correctness of the previous diag-

noses of the buried AGNs (Imanishi et al. 2007, 2016, 2018, 2019; Imanishi & Nakanishi 2014).

5.2 Interpretation of statistical trends

In Section 4.5, we report that radio spectral indices are not related to the NIR colour index, $(J-K)$, which depends on the dust temperature representing AGN activity (Figure 7). This result is interpreted as the absence of statistical contribution of AGN activity to the radio spectra of ULIRGs, which is also reported by Clemens et al. (2008). This is consistent with the prediction by the FIR-to-radio ratio, whose small value compared to other objects is treated as an outlier suggesting the presence of radio-loud AGNs (Condon et al. 1991; Yun et al. 2001), but no such object is found in our sample (Figure 5). Although a possible contribution from radio-loud AGNs can be assumed for our sample selected by buried AGNs, no hints of radio-loud AGNs are statistically obtained at this moment. Hence, our statistical results

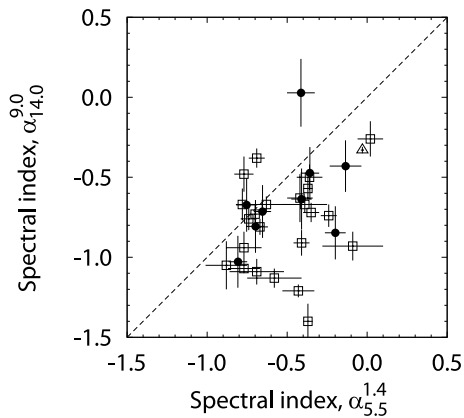


Figure 3. A comparison between low- and high-frequency spectral indices. The dashed line indicates where the spectral index is same at both frequency ranges. Filled circles indicate our results, which are based on spectral indices between 1.4 and 5.5 GHz, and between 9.0 and 14.0 GHz ($\alpha_{5.5}^{1.4}$ and $\alpha_{14.0}^{9.0}$, respectively). The Pearson correlation coefficient is 0.447 with a p-value of 0.228. Results of the entire ULIRGs (Clemens et al. 2008) are also shown by open squares, which are based on spectral indices between 1.4 and 4.8 GHz, and between 8.4 and 22.5 GHz. An open triangle shows Mrk 231 provided by the same author. Excluding Mrk 231, the Pearson correlation coefficient is 0.272 with a p-value of 0.178.

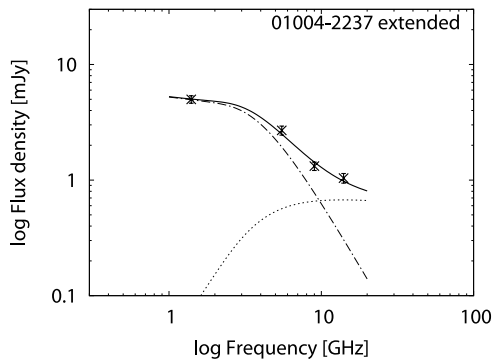


Figure 4. Radio spectrum of extended emission from IRAS 01004–2237 obtained by our observations. Observed data (crosses) and best-fit model for the spectrum presented by Equation 1 (solid line) are indicated. Model has a nonthermal component absorbed by thermal plasma with free-free emission. Thermal component (dotted line) and nonthermal component (dot-dashed line) are also indicated.

are primarily explained by other phenomena such as star formation and/or merger activity.

Generally, radio emission from starburst galaxies comes from a mixture of thermal and nonthermal plasma. In the radio regime, the former produces FFE and FFA that dominate at higher and lower frequencies, respectively (Condon et al. 1991). Since both mechanisms share the origin, the correlation of spectral indices can be assumed between these frequency ranges but have not been found. One possible explanation is a geometric effect (Clemens et al. 2008). For fixed ionising luminosity, the strength of FFE at high frequency (an optically thin regime) does not depend on the size of the ionising source in the centre, whereas the FFA found at low frequency (an optically thick regime) becomes severe if the synchrotron-emitting plasma in the centre is compact. Therefore, the lack of correlation between $\alpha_{5.0}^{1.4}$ and some physical quantities are easily explained by the fact that the central object has a variety of sizes (cf. Murphy et al.

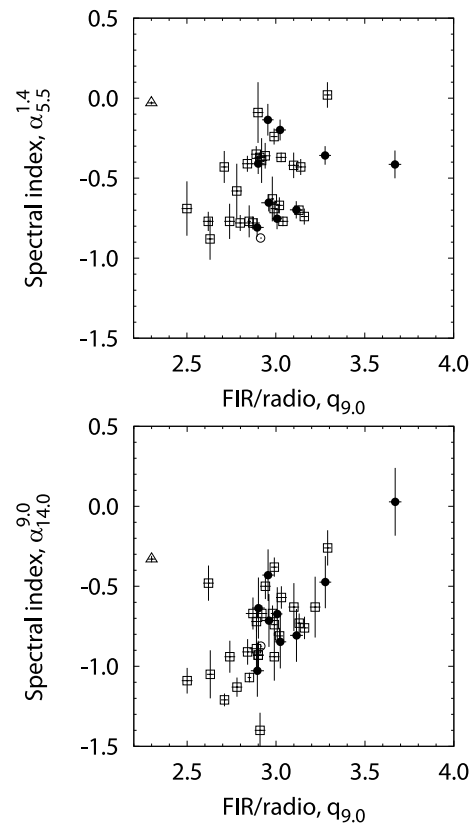


Figure 5. A comparison between FIR-to-radio ratio and radio spectral indices. Filled circles indicate our results, which are based on FIR-to-radio ratio at 9.0 GHz, $q_{9.0}$. Data points indicated by open circles represent IRAS 04103–2838, whose spectral indices and $q_{9.0}$ were calculated by interpolation from flux densities at 1.4 and 14.0 GHz. We exclude this source to calculate following statistical values. Results of the entire ULIRGs (Clemens et al. 2008) are also shown by open squares, which are based on FIR-to-radio ratio at 8.4 GHz. An open triangle shows Mrk 231 provided by the same author, which is excluded to calculate following statistical values. **(Top)** A comparison with low-frequency data. Our results are based on spectral index between 1.4 and 5.5 GHz, $\alpha_{5.5}^{1.4}$, while previous ones are based on spectral index between 1.4 and 4.8 GHz. Pearson correlation coefficients for our and previous data are 0.179 and 0.408 with p-values of 0.038 and 0.645, respectively. The difference between these coefficients is not significant with p-value of 0.581. **(Bottom)** A comparison with high-frequency data. Our results are based on spectral index between 9.0 and 14.0 GHz, $\alpha_{14.0}^{9.0}$, while previous ones are based on spectral index between 8.4 and 22.5 GHz. Pearson correlation coefficients for our and previous data are 0.806 and 0.518 with p-values of 0.005 and 0.009, respectively. The difference between these coefficients is not significant with p-value of 0.234.

2013; Barcos-Muñoz et al. 2017). This picture is consistent with a larger scatter of the flux densities at lower frequencies (Figure 8).

Assuming that most radio emission originates from starburst activity even in ULIRGs with a buried AGN (i.e. moderate AGN affects MIR features but not radio emission), both FIR emission and FFE are measures of ongoing starbursts, while synchrotron emission is an indicator of past starbursts that lag behind the lifetime of massive main-sequence stars ($\sim 10^7$ yrs). Thus, the FIR-to-radio ratio, $q_{9.0}$, and the ratio of thermal to nonthermal components, H , can decrease and the spectral index at high frequency, $\alpha_{14.0}^{9.0}$, can become more negative (i.e. steeper) as the age of the star formation increases. As discussed in Clemens et al. (2008), this scenario explains the relation between $q_{9.0}$ and $\alpha_{14.0}^{9.0}$ (Figure 5).

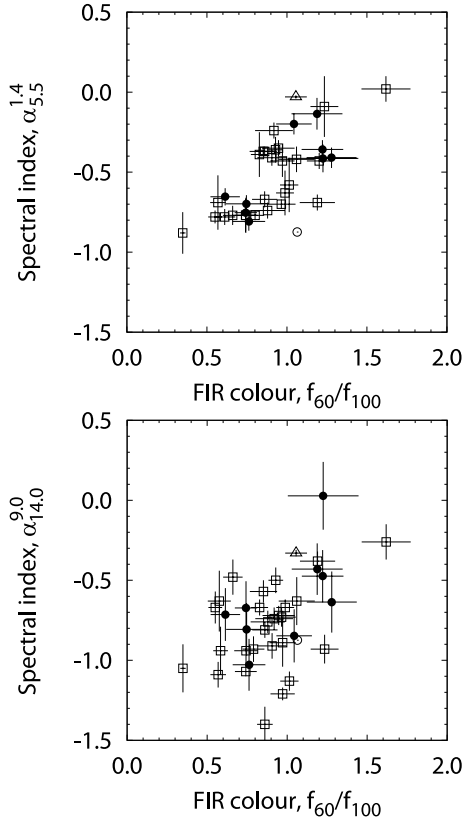


Figure 6. A comparison between FIR colour, f_{60}/f_{100} , and radio spectral indices. Filled circles indicate our results. Data points indicated by open circles represent IRAS 04103–2838, whose spectral indices were calculated by interpolation from flux densities at 1.4 and 14.0 GHz. We exclude this source to calculate following statistical values. Results of the entire ULIRGs (Clemens et al. 2008) are also shown by open squares. An open triangle shows Mrk 231 provided by the same author, which is excluded to calculate following statistical values. **(Top)** A comparison with low-frequency data. Our results are based on spectral index between 1.4 and 5.5 GHz, $\alpha_{5.5}^{1.4}$, while previous ones are based on spectral index between 1.4 and 4.8 GHz. Pearson correlation coefficients for our and previous data are 0.793 and 0.730 with p-values of 0.011 and <0.001 , respectively. The difference between these coefficients is not significant with p-value of 0.740. **(Bottom)** A comparison with high-frequency data. Our results are based on spectral index between 9.0 and 14.0 GHz, $\alpha_{14.0}^{9.0}$, while previous ones are based on spectral index between 8.4 and 22.5 GHz. Pearson correlation coefficients for our and previous data are 0.618 and 0.412 with p-values of 0.076 and 0.029, respectively. The difference between these coefficients is not significant with p-value of 0.532.

Accepting that the strength of FFA depends on the compactness of the central object, a correlation between f_{60}/f_{100} and $\alpha_{5.0}^{1.4}$ (Figure 6) suggests that the most compact sources are those in which the dust is the warmest. As suggested by Vega et al. (2005), the FIR and MIR colours of galaxies change with the age of the starburst. Figure 9 shows their evolution scenario, where the temperature of the dust in galaxies rises as the starburst peaks but then gradually decreases. This change in FIR colour is not monotonic. However, because our sample does not include objects belonging to the early starburst phase (a) in the evolutionary model, the dust temperature of the sample is considered to be in the path of the monotonic decrease. Therefore, if the temperature decreases as the central source becomes large, then the correlation between f_{100}^{60} and $\alpha_{5.0}^{1.4}$ is owing to the evolution. One explanation is the outward propagation of a ring of star formation (Alonso-Herrero et al. 2001; Väisänen et al. 2012).

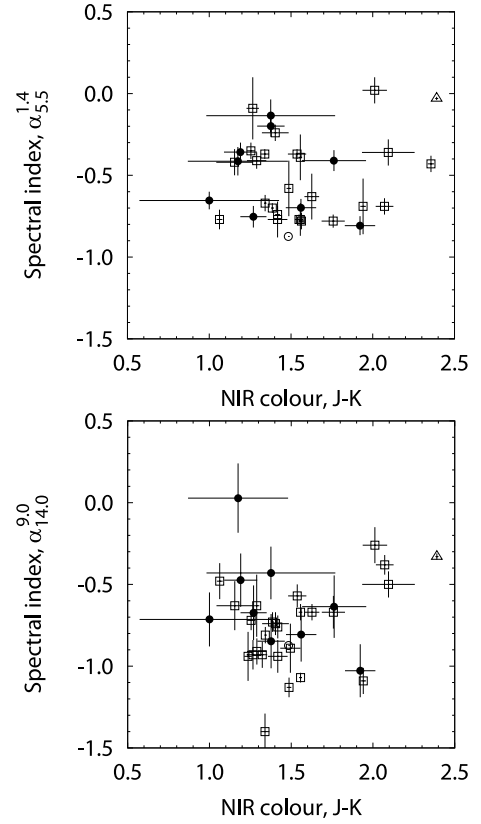


Figure 7. A comparison between NIR colour, $(J - K)$, and radio spectral indices. Filled circles indicate our results. Data points indicated by open circles represent IRAS 04103–2838, whose spectral indices were calculated by interpolation from flux densities at 1.4 and 14.0 GHz. We exclude this source to calculate following statistical values. Results of the entire ULIRGs (Clemens et al. 2008) are also shown by open squares. An open triangle shows Mrk 231 provided by the same author, which is excluded to calculate following statistical values. **(Top)** A comparison with low-frequency data. Our results are based on spectral index between 1.4 and 5.5 GHz, $\alpha_{5.5}^{1.4}$, while previous ones are based on spectral index between 1.4 and 4.8 GHz. Pearson correlation coefficients for our and previous data are -0.225 and -0.290 with p-values of 0.561 and 0.151, respectively. The difference between these coefficients is not significant with p-value of 0.879. **(Bottom)** A comparison with high-frequency data. Our results are based on spectral index between 9.0 and 14.0 GHz, $\alpha_{14.0}^{9.0}$, while previous ones are based on spectral index between 8.4 and 22.5 GHz. Pearson correlation coefficients for our and previous data are -0.526 and -0.080 with p-values of 0.145 and 0.686, respectively.

Note that, at the same time f_{100}^{60} and $\alpha_{5.0}^{1.4}$ do not correlate with $\alpha_{14.0}^{9.0}$ and $q_{9.0}$, respectively, which are measures of the starburst age if we assume a starburst dominant radio spectrum. Combined with the fact that the size of the star-forming regions may vary from object to object, the age might be only a secondary factor to explain the strength of FFA.

In addition to star formation, merger activity can also affect the radio properties of ULIRGs. Murphy (2013) reports relations of the radio properties to merger stages classified by Haan et al. (2011). As the merger stage progresses, the excess radio emission relative to a prediction from the FIR to radio correlation increases and the radio spectrum at high frequency becomes steeper. The author suggests that these features found in ongoing merger activity arise from radio bridges and tidal tails similar to what is observed for UGC 12914/5 (Condon et al. 1993). If this is the case, a correlation between the high-frequency spectral index and the FIR-to-radio ratio

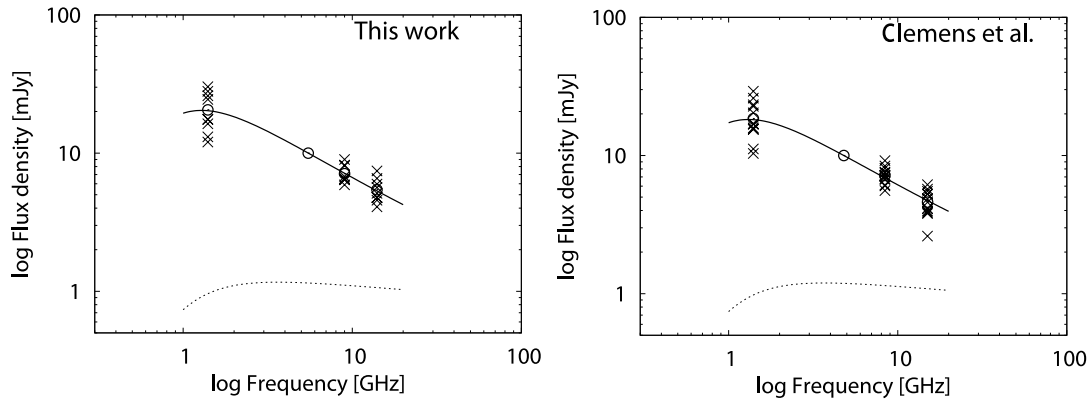


Figure 8. Normalised composite spectra of our targets (left) and sample from Clemens et al. (2008) (right). Crosses and open circles show the flux densities of each source and their average flux densities, respectively. We fix flux densities at the C band to 10 mJy, whose observed frequencies are 5.5 and 4.8 GHz for our targets and sample from Clemens et al. (2008), respectively. Solid and dotted lines indicate the best-fit model for the spectra presented by Equation 1 and its thermal component, respectively. Because of the small thermal fraction, the solid line overlaps the nonthermal component.

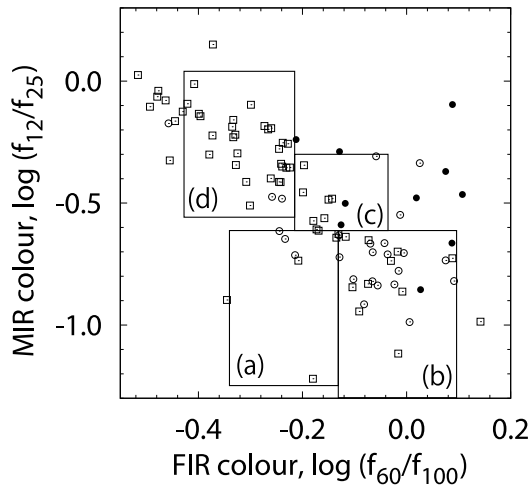


Figure 9. IRAS Colour-colour diagrams. Horizontal and vertical axes indicate MIR colour f_{12}/f_{25} , and FIR colour f_{60}/f_{100} , respectively. Samples from Dale et al. (2000), Clemens et al. (2008) and ours are indicated by open squares, open circles, and filled circles, respectively. Four closed regions (a)–(d) highlight four main evolutionary phases of the starburst models proposed by Vega et al. (2005), where galaxies transition from (a) to (d).

due to merger activity is supposed, which is certainly found in Figure 5. In contrast, although low-frequency spectra are found to flatten during the merger process, no relation is found between the low-frequency spectral index and the FIR-to-radio ratio. Because spectral features at lower frequencies are considered to come from the vicinity of the compact starburst (Murphy et al. 2013), the lack of the correlation suggests diversity in the optical depth of the FFA screen hiding the central object.

5.3 Contribution of AGNs to individual objects

In Section 5.2, we find that a hint of AGNs is not suggested by the distribution of the FIR-to-radio ratio where no outlier is found, and by the statistical relation between the NIR colour, $(J - K)$, and radio spectral indices. The buried AGN found at MIR and submillimetre wavelengths could be considered not to be the main contributors to the radio emission, and hence the radio spectra can be statistically explained by star formation and/or merger activity to some extent

(e.g., Clemens et al. 2010; Murphy 2013). However, the situation is much more complicated because $(J - K)$ is not determined by heating from AGNs alone but is also affected by dust extinction, and because only galaxies containing radio-loud AGNs have FIR-to-radio ratios distinguishable from those of the starforming galaxies (Murphy 2009; Morić et al. 2010). Moreover, at this moment, the factors that determine the radio loudness of AGNs are still not obvious in individual sources. Therefore, the contribution of another radiative process typically seen in AGNs can still be considered, and the statistical properties and explanations referred to thus far cannot completely rule out the existence of AGNs at radio.

5.3.1 GHz-peaked spectrum

Generally, AGNs show strong synchrotron radiation whose radio spectrum becomes steep if the sources are optically thin while peaked or inverted if they suffer from FFA or synchrotron self-absorption owing to a strong magnetic field (e.g. Tornaiainen et al. 2005; Orienti & Dallacasa 2008). In Figure 2, the nonthermal components of IRAS 00091–0738, IRAS 01004–2237, and IRAS 01298–0744 show a GHz-peaked spectrum. Although supernova remnants show similar peaked spectra (e.g. Allen & Kronberg 1998; Chandra et al. 2004), such a spectrum from AGNs has also been found in ULIRGs (e.g. Gallimore & Beswick 2004; Hagiwara et al. 2011), and thus these objects are still probable candidates for AGNs. Nevertheless, as our observed frequencies are limited to the GHz ranges, the results of the model fit can be different if data at lower frequencies are included (e.g. Chandra et al. 2004). In reality, many of the spectra, including low-frequency data, indicate the presence of an additional component peaked at frequencies below 1 GHz (Clemens et al. 2010; Galvin et al. 2018). To confirm the presence of the GHz-peaked spectrum from the nonthermal component, observations at lower frequencies are required.

Confirmation of a high brightness temperature of more than 10^{10} K found in sources with synchrotron self-absorption is also important for identifying AGNs (Broderick & Condon 1975). The direct measurement of the temperature is the best method, but since the angular resolution of this study is limited, this would be accomplished by future observations with long baselines. An alternative to high-resolution observation is testing the source variability (e.g. Zhou et al. 2006; Ghosh & Punjly 2007). Although we do not find any significant changes in the sources (Section 4.2), it is insufficient

to conclude that the sources are stable because only two-epoch data are available at the moment.

5.3.2 Steepening at high frequency

Based on the model given by Equation 1, the radio spectrum should flatten at higher frequencies because the contribution of thermal emission showing $\alpha \sim -0.1$ dominates with increasing frequency. However, in the spectra of IRAS 00091–0738, IRAS 00188–0856, and IRAS 01298–0744, we find steepening toward higher frequencies (see $\alpha_{9.0}^{5.5}$ and $\alpha_{14.0}^{9.0}$ in Table 5). A similar feature is also reported by several authors, whose origin has been debated (Clemens et al. 2008, 2010; Leroy et al. 2011; Murphy 2013).

One explanation is spectral ageing owing to the energy loss of relativistic electrons, which increases with increasing particle energy, resulting in a change in the spectral slope of $\Delta\alpha \sim 0.5$ across the so-called break frequency (Kardashev 1962; Pacholczyk 1970; Jaffe & Perola 1973). Clemens et al. (2008) considered that the summation of several components with different break frequencies, in general, produced a straight and monotonic spectrum. There, stochastic effects such as variations in the supernovae rate might cause the break, but this is not probable because even the brightest supernova remnants contribute only $< 10\%$ of the total emission from ULIRG’s nuclei (e.g. Lonsdale et al. 2006). However, synchrotron ageing can still explain the spectral break if we consider nonthermal plasma from AGNs whose contribution becomes potentially well over 10%. In particular, large nonthermal fractions (Figure 2) are found in IRAS 00091–0738 and IRAS 00188–0856, which are probable candidates for sources with radio AGNs. Although at ~ 30 GHz the presence of a predominant thermal component is found for typical ULIRGs (Barcos-Muñoz et al. 2017), the AGN candidates reported here might suggest a significant contribution of a nonthermal component at the frequency. Therefore, as suggested by Leroy et al. (2011), the detection of spectral breaks can still be a way to distinguish AGNs from starbursts. We note that, while an instantaneous injection model is preferred if multifrequency images with the sufficiently high spatial resolution are available (e.g. Nagai et al. 2006), a continuous injection model is supposed for unresolved sources, whose break does not disappear even if several components of different spectral ages are superposed (e.g. Murgia et al. 1999; Murgia 2003).

In addition to the above, some authors have made other arguments. Clemens et al. (2010) has proposed that the ionisation loss that gradually flattens radio spectra at lower frequencies explained the spectral break (Thompson et al. 2006). Nevertheless, some of their sample at the same time show a highly steep spectral index of $\alpha < -1$ at high frequency (Clemens et al. 2008), which still requires the synchrotron ageing of nonthermal plasma as found in AGNs. On another hand, a consideration made by Murphy (2013) has not only explained the spectral break but also the highly steep spectral index. As referred in Section 5.2, they have reported that as the merger stage of merging galaxy pairs progresses radio bridges and tidal tails of ongoing mergers start to show a steep spectral index at high frequency, which is caused by rapid synchrotron ageing in a magnetised medium produced by the dynamical interaction. This scenario could be the case for IRAS 00091–0738 and IRAS 01298–0744, whose tidal tails are optically confirmed by Veilleux et al. (2002). In contrast, the optical image of IRAS 00188–0856 provided by the same authors does not show any signs of tidal tails or disturbed morphology. In contrast, the optical image of IRAS 00188–0856 provided by the same authors does not show any signs of tidal tails or disturbed morphology. We do not find any traces of merger activity at least in the optical image

and thus another explanation like an AGN is still considerable for IRAS 00188–0856.

5.3.3 Extended emission in IRAS 01004–2237

IRAS 01004–2237 shows extended features across ~ 50 arcsec, which corresponds to the projected linear size of ~ 100 kpc (Figure 1). A few arcseconds away from the northeast component, we find a faint point source in an optical image provided by the Pan-STARRS (Chambers et al. 2016) whose colour suggests a galaxy at $0.6 < z < 1.0$ (cf. Prakash et al. 2015), while the southwest one has no counterpart, which should be associated with IRAS 01004–2237 itself. Its symmetrical structure including the northeast component evokes FR2 radio galaxies (Fanaroff & Riley 1974).

While most ULIRGs generally constitute merger systems, IRAS 01004–2237 itself does not indicate the implication of recent merger activity in the form of tidal tails or loops (Veilleux et al. 2002). In addition, although its luminosity does not meet the criteria, the source has a nearly stellar radial profile similar to that of quasars (Surace et al. 1998). Furthermore, Veilleux et al. (1999) classified the source as H II once, but Yuan et al. (2010) and Rodríguez Zaurín et al. (2013) identify the optical AGN signature by decomposing its emission lines into multiple components. Combined with the diagnostic result at MIR (Imanishi et al. 2007; Veilleux et al. 2009; Nardini et al. 2010), the presence of an AGN in the nucleus of IRAS 01004–2237 is certain, which supports the AGN origin of the extended radio emission.

On the other hand, the extended emission could also be considered as a radio mini-halo or a radio relic associated with galaxy clusters (Feretti et al. 2012; van Weeren et al. 2019). These are usually located in the centre of merging clusters and are accompanied by a hot ionised intracluster medium that emits X-rays with the same spread as radio. However, we do not found such a feature by X-ray observations (Voges et al. 1999; Teng et al. 2005); hence, the extended emission is not induced by the merger.

Regardless of whether the extended feature originates from an AGN or a merger activity, an interpretation of the radio spectrum (Figure 4) is still unknown. At high frequency, nonthermal plasma having lost the energy generally shows a steep spectrum indicating $\alpha \lesssim -1$, or up to ~ -2 (Parma et al. 2007; Brunetti et al. 2008; Orienti et al. 2010; Murgia et al. 2011). By contrast, the spectrum of the extended component associated with IRAS 01004–2237 shows flattening at high frequency, which suggests a significant contribution of the thermal plasma. However, this kind of feature has not been reported for both AGN or merger activities. We must pay attention to the interpretation of this data because this result could be an artificial one. Since the spatial resolution of the images at 5.5 and 14.0 GHz is approximately two times lower than that at 9.0 GHz (Table 4), our observation can resolve out the diffuse extended feature at 9.0 GHz and then underestimate the flux density. We need deep observation to obtain a conclusive result before making further discussions.

6 CONCLUSIONS

We conducted new multifrequency VLA observations for ULIRGs whose AGNs are not found at optical wavelengths but are identified at MIR or submillimetre wavelengths (Imanishi et al. 2007, 2016, 2018, 2019; Imanishi & Nakanishi 2014). This was made for shedding light on the contribution of buried AGNs to radio emission of ULIRGs through a comparison with the observational results obtained by

Clemens et al. (2008), whose sample is based on the entire ULIRGs. The main conclusions of this study can be summarised as follows.

(i) The spectral indices at low and high frequencies are not related to each other. The spectral index at high frequency significantly correlates with the FIR-to-radio ratio at 9.0 GHz while no relation is found at low frequency. In contrast, the spectral index at low frequency significantly correlates with the FIR colour while no relation is found at high frequency. These statistical trends are similar to those of the entire ULIRGs provided by Clemens et al. (2008).

(ii) The statistical similarity mentioned above suggests that all ULIRGs have common radiative processes at radio regardless of the presence of optical AGNs. Thus, whereas the radio spectra of our targets can be mainly explained by starbursts and/or merger activity (Clemens et al. 2010; Murphy 2013), combined with the AGN diagnosis by MIR and submillimetre spectroscopy it might be possible that AGNs contribute equally to the radio emissions of every ULIRG.

(iii) Some individual sources imply contributions from AGNs. IRAS 00188–0856 not indicating disturbed morphology at optical wavelengths shows a high nonthermal fraction and a spectral break at high frequency, which can be explained by synchrotron ageing of nonthermal plasma emitted from AGNs. In addition, 100-kpc scale extended radio emission is associated with IRAS 01004–2237, whose two-sided morphology and no X-ray detection suggest that this system is not induced by a merger in a cluster but originates from AGN activity.

ACKNOWLEDGEMENT

We wish to express our appreciation to an anonymous reviewer for the insightful comments helping us significantly improve the paper and make a solid discussion. The VLA is a facility of NRAO, operated by Associated University Inc. under cooperative agreement with the National Science Foundation. This publication makes use of data products from the Two Micron All Sky Survey, which is a joint project of the University of Massachusetts and the Infrared Processing and Analysis Center/California Institute of Technology, funded by the National Aeronautics and Space Administration and the National Science Foundation. We also made use of the NASA/IPAC Extragalactic Database operated by the Jet Propulsion Laboratory, California Institute of Technology. This work was partially supported by a Grant-in-Aid for Scientific Research (B; 24340042) from the Japanese Ministry of Education, Culture, Sports, Science and Technology. We thank Editage (www.editage.com) for English language editing.

DATA AVAILABILITY

Data underlying this article are available in NRAO Science Data Archive, at <https://archive.nrao.edu/archive/advquery.jsp>. The reduced data by authors will be shared on reasonable request to the corresponding author.

REFERENCES

- Allen M. L., Kronberg P. P., 1998, *ApJ*, **502**, 218
- Alonso-Herrero A., Engelbracht C. W., Rieke M. J., Rieke G. H., Quillen A. C., 2001, *ApJ*, **546**, 952
- Armus L., et al., 2004, *ApJS*, **154**, 178
- Armus L., et al., 2007, *ApJ*, **656**, 148
- Barcos-Muñoz L., et al., 2017, *ApJ*, **843**, 117
- Becker R. H., White R. L., Helfand D. J., 1995, *ApJ*, **450**, 559
- Broderick J. J., Condon J. J., 1975, *ApJ*, **202**, 596
- Brunetti G., et al., 2008, *Nature*, **455**, 944
- Chambers K. C., et al., 2016, arXiv e-prints, p. arXiv:1612.05560
- Chandra P., Ray A., Bhatnagar S., 2004, *ApJ*, **604**, L97
- Clemens M. S., Vega O., Bressan A., Granato G. L., Silva L., Panuzzo P., 2008, *A&A*, **477**, 95
- Clemens M. S., Scaife A., Vega O., Bressan A., 2010, *MNRAS*, **405**, 887
- Condon J. J., Huang Z. P., Yin Q. F., Thuan T. X., 1991, *ApJ*, **378**, 65
- Condon J. J., Helou G., Sanders D. B., Soifer B. T., 1993, *AJ*, **105**, 1730
- Condon J. J., Cotton W. D., Greisen E. W., Yin Q. F., Perley R. A., Taylor G. B., Broderick J. J., 1998, *AJ*, **115**, 1693
- Cutri R. M., et al., 2003, VizieR Online Data Catalog, p. II/246
- Dale D. A., et al., 2000, *AJ*, **120**, 583
- Fanaroff B. L., Riley J. M., 1974, *MNRAS*, **167**, 31P
- Feretti L., Giovannini G., Govoni F., Murgia M., 2012, *A&A Rev.*, **20**, 54
- Gallimore J. F., Beswick R., 2004, *AJ*, **127**, 239
- Galvin T. J., et al., 2018, *MNRAS*, **474**, 779
- Ghosh K. K., Punsly B., 2007, *ApJ*, **661**, L139
- Haan S., et al., 2011, *AJ*, **141**, 100
- Hagiwara Y., Baan W. A., Klöckner H.-R., 2011, *AJ*, **142**, 17
- Helou G., Soifer B. T., Rowan-Robinson M., 1985, *ApJ*, **298**, L7
- Imanishi M., 2009, *ApJ*, **694**, 751
- Imanishi M., Nakanishi K., 2014, *AJ*, **148**, 9
- Imanishi M., Dudley C. C., Maloney P. R., 2006, *ApJ*, **637**, 114
- Imanishi M., Dudley C. C., Maiolino R., Maloney P. R., Nakagawa T., Risaliti G., 2007, *ApJS*, **171**, 72
- Imanishi M., Nakagawa T., Ohyama Y., Shirahata M., Wada T., Onaka T., Oi N., 2008, *PASJ*, **60**, 489
- Imanishi M., Maiolino R., Nakagawa T., 2010a, *ApJ*, **709**, 801
- Imanishi M., Nakagawa T., Shirahata M., Ohyama Y., Onaka T., 2010b, *ApJ*, **721**, 1233
- Imanishi M., Nakanishi K., Izumi T., 2016, *AJ*, **152**, 218
- Imanishi M., Nakanishi K., Izumi T., 2018, *ApJ*, **856**, 143
- Imanishi M., Nakanishi K., Izumi T., 2019, *ApJS*, **241**, 19
- Jaffe W. J., Perola G. C., 1973, *A&A*, **26**, 423
- Kardashev N. S., 1962, *Soviet Ast.*, **6**, 317
- Kauffmann G., et al., 2003, *MNRAS*, **346**, 1055
- Kewley L. J., Heisler C. A., Dopita M. A., Lumsden S., 2001, *ApJS*, **132**, 37
- Kim D. C., Sanders D. B., 1998, *ApJS*, **119**, 41
- Leroy A. K., et al., 2011, *ApJ*, **739**, L25
- Lister M. L., 2001, *ApJ*, **561**, 676
- Lonsdale C. J., Diamond P. J., Thrall H., Smith H. E., Lonsdale C. J., 2006, *ApJ*, **647**, 185
- Maiolino R., et al., 2003, *MNRAS*, **344**, L59
- McMullin J. P., Waters B., Schiebel D., Young W., Golap K., 2007, in Shaw R. A., Hill F., Bell D. J., eds, *Astronomical Society of the Pacific Conference Series Vol. 376, Astronomical Data Analysis Software and Systems XVI*, p. 127
- Morić I., Smolčić V., Kimball A., Riechers D. A., Ivezić Ž., Scoville N., 2010, *ApJ*, **724**, 779
- Moshir M., et al. 1990, IRAS Faint Source Catalogue, p. 0
- Murgia M., 2003, *PASA*, **20**, 19
- Murgia M., Fanti C., Fanti R., Gregorini L., Klein U., Mack K. H., Vigotti M., 1999, *A&A*, **345**, 769
- Murgia M., et al., 2011, *A&A*, **526**, A148
- Murphy E. J., 2009, *ApJ*, **706**, 482
- Murphy E. J., 2013, *ApJ*, **777**, 58
- Murphy E. J., Stierwalt S., Armus L., Condon J. J., Evans A. S., 2013, *ApJ*, **768**, 2
- Nagai H., Inoue M., Asada K., Kamenoi S., Doi A., 2006, *ApJ*, **648**, 148
- Nardini E., Risaliti G., Salvati M., Sani E., Imanishi M., Marconi A., Maiolino R., 2008, *MNRAS*, **385**, L130
- Nardini E., Risaliti G., Salvati M., Sani E., Watabe Y., Marconi A., Maiolino R., 2009, *MNRAS*, **399**, 1373
- Nardini E., Risaliti G., Watabe Y., Salvati M., Sani E., 2010, *MNRAS*, **405**, 2505
- Orienti M., Dallacasa D., 2008, *A&A*, **487**, 885

- Orienti M., Murgia M., Dallacasa D., 2010, *MNRAS*, **402**, 1892
- Pacholczyk A. G., 1970, Radio astrophysics. Nonthermal processes in galactic and extragalactic sources
- Parma P., Murgia M., de Ruiter H. R., Fanti R., Mack K. H., Govoni F., 2007, *A&A*, **470**, 875
- Prakash A., Licquia T. C., Newman J. A., Rao S. M., 2015, *ApJ*, **803**, 105
- Rodríguez Zaurín J., Tadhunter C. N., Rose M., Holt J., 2013, *MNRAS*, **432**, 138
- Sanders D. B., Mirabel I. F., 1996, *ARA&A*, **34**, 749
- Skrutskie M. F., et al., 2006, *AJ*, **131**, 1163
- Soifer B. T., Boehmer L., Neugebauer G., Sanders D. B., 1989, *AJ*, **98**, 766
- Soifer B. T., et al., 2000, *AJ*, **119**, 509
- Spoon H. W. W., Moorwood A. F. M., Lutz D., Tielens A. G. G. M., Siebenmorgen R., Keane J. V., 2004, *A&A*, **414**, 873
- Surace J. A., Sanders D. B., Vacca W. D., Veilleux S., Mazzarella J. M., 1998, *ApJ*, **492**, 116
- Teng S. H., Wilson A. S., Veilleux S., Young A. J., Sanders D. B., Nagar N. M., 2005, *ApJ*, **633**, 664
- Thompson T. A., Quataert E., Murray N., 2005, *ApJ*, **630**, 167
- Thompson T. A., Quataert E., Waxman E., Murray N., Martin C. L., 2006, *ApJ*, **645**, 186
- Torniaainen I., Tornikoski M., Teräsraanta H., Aller M. F., Aller H. D., 2005, *A&A*, **435**, 839
- Väisänen P., Rajpaul V., Zijlstra A. A., Reunanen J., Kotilainen J., 2012, *MNRAS*, **420**, 2209
- Vega O., Silva L., Panuzzo P., Bressan A., Granato G. L., Chavez M., 2005, *MNRAS*, **364**, 1286
- Veilleux S., Osterbrock D. E., 1987, *ApJS*, **63**, 295
- Veilleux S., Kim D. C., Sanders D. B., 1999, *ApJ*, **522**, 113
- Veilleux S., Kim D. C., Sanders D. B., 2002, *ApJS*, **143**, 315
- Veilleux S., et al., 2009, *ApJS*, **182**, 628
- Voges W., et al., 1999, *A&A*, **349**, 389
- Yuan T. T., Kewley L. J., Sanders D. B., 2010, *ApJ*, **709**, 884
- Yun M. S., Reddy N. A., Condon J. J., 2001, *ApJ*, **554**, 803
- Zhou H., Wang T., Wang H., Wang J., Yuan W., Lu Y., 2006, *ApJ*, **639**, 716
- van Weeren R. J., de Gasperin F., Akamatsu H., Brügggen M., Feretti L., Kang H., Stroe A., Zandanel F., 2019, *Space Sci. Rev.*, **215**, 16

This paper has been typeset from a $\text{\TeX}/\text{\LaTeX}$ file prepared by the author.